RSC Advances

COMMUNICATION

View Article Online
View Journal | View Issue

Cite this: *RSC Adv.*, 2015, **5**, 29353

Received 31st December 2014
Accepted 9th March 2015

DOI: 10.1039/c4ra17300g

www.rsc.org/advances

Highly efficient removal of NO with ordered mesoporous manganese oxide at low temperature†

Sihui Zhan,*[a] Dandan Zhu,[a] Mingying Qiu,[a] Hongbing Yu[a] and Yi Li*[b]

Highly ordered mesoporous MnO_2 was prepared using KIT-6 as a hard template, for selective catalytic reduction (SCR) of NO with NH_3 at low temperature, which was characterized using TEM, XRD, BET, XPS, H_2-TPR, NH_3-TPD and *in situ* DRIFT. Based on the results of HRTEM, the ordered mesoporous channels of MnO_2 can be observed clearly. The SCR activity of NO with NH_3 at low temperature was evaluated using these ordered mesoporous MnO_2 as catalysts, and it was found that 100% NO conversion efficiency could be achieved at temperatures from 150 to 250 °C. For comparison, mesoporous Mn_2O_3 and bulk MnO_2 were synthesized and their NO conversions were tested using the same parameters. The mechanism of improved SCR performance was investigated using XPS, H_2-TPR, NH_3-TPD and *in situ* DRIFT, and it was indicated that specific surface area, surface chemisorbed oxygen, reducibility and acid sites have great effect on the SCR reaction. In addition, the effects of H_2O and GHSV on NO conversion were investigated.

1 Introduction

Nitrogen oxide (NO) originating from industrial combustion of coal and fossil fuel has severe effects on the atmospheric environment, such as photo-chemical smog, acid rain and ozone depletion, which have raised wide concern because of the high toxicity to human health.[1,2] Among many approaches for removing NO, selective catalytic reduction (SCR) degradation of NO with NH_3 is considered to be one of the most efficient and widely used methods. Until now, commercial V_2O_5–WO_3/TiO_2 catalysts have been used in the SCR field; however, the higher working temperature from 300 to 400 °C means that the reaction device of the SCR unit must be located upstream of the electrostatic precipitator, which can cause problems, such as inactivation, catalyst agglomeration and higher cost.[3,4] If we wish to avoid these problems by locating the VWTi SCR reactor downstream of the electrostatic precipitator, it is necessary to preheat the flue gas higher than 200 °C. Therefore, there is a need for development of a novel low-temperature SCR catalyst to overcome these problems.

According to previous reports, Mn-based catalysts show excellent SCR activity at low temperature by doping transition metal oxides into MnOx, such as MnOx/CeO_2,[4] MnOx/TiO_2,[5] MnOx/CuO[6,7] and MnOx/Fe.[8] However, the SCR activity of pure MnO_2 is poor, and no corresponding research has been done to improve its degradation efficiency. As is already known, the SCR removal performance of NO can be affected by the oxidation state of manganese, the crystallinity and the specific surface.[9] For example, Yang found that MnO_2 nanorods had higher activity for reducing NO than did MnO_2 nanotubes and nanoparticles, because of their low crystallinity, higher lattice oxygen, high reducibility and stronger acid sites.[10]

Since the discovery of MCM-41 and SBA-15, mesoporous materials have attracted interest because of their large specific surface area, interconnected channels and well defined pore diameters.[11,12] These hierarchical structures have been found to be beneficial for generation of abundant active sites and mass transfer, enabling the effective reduction of NO.[13–15] Recently, mesoporous MnO_2 has been prepared and applied in many fields such as lithium-ion batteries,[16] supercapacitors[17] and catalytic domain.[18] However, to our knowledge, there is no report of use of mesoporous MnO_2 for SCR removal of NO with NH_3 at low temperature.

In this paper, highly ordered pure mesoporous MnO_2 was successfully prepared through a nanocasting method using KIT-6 as template, and characterized by TEM, XRD, BET, H_2-TPR, NH_3-TPD, XPS and *in situ* DRIFT. In addition, the SCR activity of NO with NH_3 at low temperature was evaluated using the ordered mesoporous MnO_2 as catalyst. Furthermore, mesoporous Mn_2O_3 and bulk MnO_2 nanoparticles were prepared

[a]*College of Environmental Science and Engineering, Key Laboratory of Environmental Pollution Process and Environmental Criteria, Nankai University, Tianjin 300071, P. R. China*

[b]*Department of Chemistry, Tianjin University, Tianjin 300072, P. R. China*

† Electronic supplementary information (ESI) available. See DOI: 10.1039/c4ra17300g

and used as SCR catalyst to clean NO with NH_3, and a possible reaction mechanism is suggested.

2 Experimental

2.1 Materials

All chemicals used here are analytical grade. The KIT-6 was prepared as described in an earlier published paper.[19] Hydrochloric acid (HCl), ethanol, *n*-butanol, sodium hydroxide (NaOH), tetraethyl orthosilicate (TEOS) were purchased from Jiangtian Chemical Technology Co. Ltd. (Tianjin, China). Both Pluronic P123 and $Mn(NO_3)_2 \cdot 4H_2O$(97%) were purchased from Sigma-Aldrich.

2.2 Catalyst preparation

The highly ordered mesoporous MnO_2 was prepared using mesoporous silica KIT-6 as a template.[20] In a typical process, 3 g of $Mn(NO_3)_2 \cdot 4H_2O$ (97%) was dissolved in 25 mL of ethanol, and then 1 g of KIT-6 was added to the solution. The mixture was stirred overnight at room temperature, the powder sample was then sintered in a muffle furnace with a heating rate of 1 °C min^{-1} from room temperature to 350 °C, and maintained at 350 °C for 5 h. After cooling to room temperature, the resulting powder was treated twice with a hot aqueous solution of 2 M NaOH to remove the silica template, followed by washing with deionized water several times and then drying at 60 °C.

The synthesis process of ordered mesoporous Mn_2O_3 was similar to that of MnO_2, with the only difference being that the obtained solid was calcined in a muffle furnace with a heating rate of 1 °C min^{-1} from room temperature to 600 °C, and maintained at 600 °C for 4 h.

As a comparison, conventional MnO_2 was prepared directly by calcining $Mn(NO_3)_2 \cdot 4H_2O$ (97%) at 350 °C for 5 h.

2.3 Characterization

The size and morphology of MnO_2 and Mn_2O_3 were observed by transmission electron microscopy (TEM) using a JEOL Model JEM-1200EX at 80 kV. The X-ray diffraction (XRD) patterns of MnO_2 were recorded *via* an X-ray diffractometer (Rigaku D/Max 2200PC) with a graphite monochromator and CuKα radiation (λ = 0.15418 nm) at room temperature, with the voltage and electric current being fixed at 28 kV and 20 mA. N_2 adsorption–desorption isotherms were recorded *via* Quantachrome AutoSorb iQ-MP. Temperature-programmed reduction of H_2 (H_2-TPR) and temperature-programmed desorption of NH_3 (NH_3-TPD) were carried out on a Micromeritics Autochem 2920 II instrument with thermal conductivity detector (TCD). The oxidation state and concentration of sample surfaces were observed using X-ray photoelectron spectroscopy (XPS, ESCALAB 250 multi-technique X-ray photoelectron spectrometer (UK)), with a monochromatic AlKα X-ray source ($h\nu$ = 1486.6 eV). All XPS spectra were recorded using an aperture slot of 300 × 700 microns, survey spectra were recorded with a pass energy of 160 eV, and high resolution spectra with a pass energy of 40 eV. The *in situ* Diffuse Reflectance Infrared Fourier Transform Spectroscopy (*in situ* DRIFTS) spectra were recorded using a Bruker Tensor 27 spectrophotometer. Prior to each experiment, the sample was heated to 350 °C in argon for 1 h and then cooled to 150 °C. The spectra were recorded using a KBr pellet method in the range of 400–4000 cm^{-1} by accumulating 32 scans at a resolution of 4 cm^{-1}.

2.4 Catalytic activity test

The SCR activity measurements were carried out in a fixed-bed quartz reactor (i.d. 10 mm), operating under atmospheric pressure at 100–350 °C. For each SCR activity test, 0.5 g of catalyst was used (pressed into blocks, and then crushed and sieved into 40–60 meshes before SCR activity measurements). The typical reaction conditions were set as follows: 0.5 g catalyst, 500 ppm NO, 500 ppm NH_3, 3% O_2, 5% H_2O (when used), all balanced by N_2 with a total gas flow rate of 200 mL min^{-1}, giving a gas hourly space velocity (GHSV) of 2.8 × 104 h^{-1}. The gas-phase concentrations of all components were measured by a FTIR spectrometer (Gasmet FTIR DX4000, Finland). NO conversion under steady-state reaction conditions for 1 h was obtained from the following equation, in which NO_{in} was the concentration of inlet NO, and NO_{out} was the concentration of outlet NO:

$$\text{NO conversion (\%)} = (1 - [NO]_{out}/[NO]_{in}) \times 100\%$$

3 Results and discussion

3.1 Characterization of catalyst

To study the microstructure of MnO_2 in detail, typical TEM images were set at different magnifications, as shown in Fig. 1. From these, the cubic mesostructure and lattice fringe of MnO_2 can be observed directly. From Fig. 1a–c, the 6.7 nm average pore diameter of MnO_2 (Fig. 1b and c) is consistent with the 5.9 nm wall thickness of KIT-6 (Fig. 1a), which indicates that cubic mesostructures of MnO_2 result from thermal decomposition of metal precursors within the confined mesochannels of the silica template.[20,21] The unit cell parameters, a_0, are 11.2 and 22.8 nm for mesoporous MnO_2 and Mn_2O_3. As illustrated in the typical HRTEM image of MnO_2 (Fig. 1d), lattice fringes of MnO_2 that belong to the (110) crystallographic planes (d = 0.341 nm) and the (101) crystallographic planes (d = 0.254 nm) can be clearly identified, demonstrating that the MnO_2 sample is highly crystalline. Furthermore, the electron diffraction patterns of the MnO_2 sample can be indexed to the highly crystalline reflections, which is in accordance with the results from XRD (described later). Comparing the TEM images of mesoporous MnO_2 (Fig. 1c) and mesoporous Mn_2O_3 (Fig. 1e), the order of mesoporous MnO_2 is better than that of mesoporous Mn_2O_3, which may be because of incomplete pore filling of precursor and relatively high volume shrinkage during the sintering process, and this is consistent with results from XRD (described later).[21,22] To evaluate the stability of mesostructure materials, characterization of TEM for the used mesoporous MnO_2 was conducted, as shown in the Fig. 1f. It is observed that the used mesoporous MnO_2 still show highly ordered

mesoporous channels after SCR test, confirming clearly the high stability of mesoporous MnO_2. In addition, energy-dispersive X-ray spectroscopy (EDS) was also conducted to analyze the chemical composition of MnO_2, which proved that MnO_2 catalysts were composed of Mn and O elements. The C and Cu peak in the EDS spectrum comes from the copper mesh used in the TEM tests, and the low levels of element Si originate from residues of the KIT-6 template.

To further study the mesostructure of samples, low-angle XRD patterns of mesoporous MnO_2 and Mn_2O_3 are shown in Fig. 2a. The characteristic reflection of the (211) plane at 2θ of around 1° for mesoporous MnO_2 can be clearly observed, corresponding to the main (211) diffraction peak of the cubic *Ia3d* symmetry of mesoporous silica template (Fig. 1S†), which indicates the highly ordered mesoporous structure of MnO_2.[23]

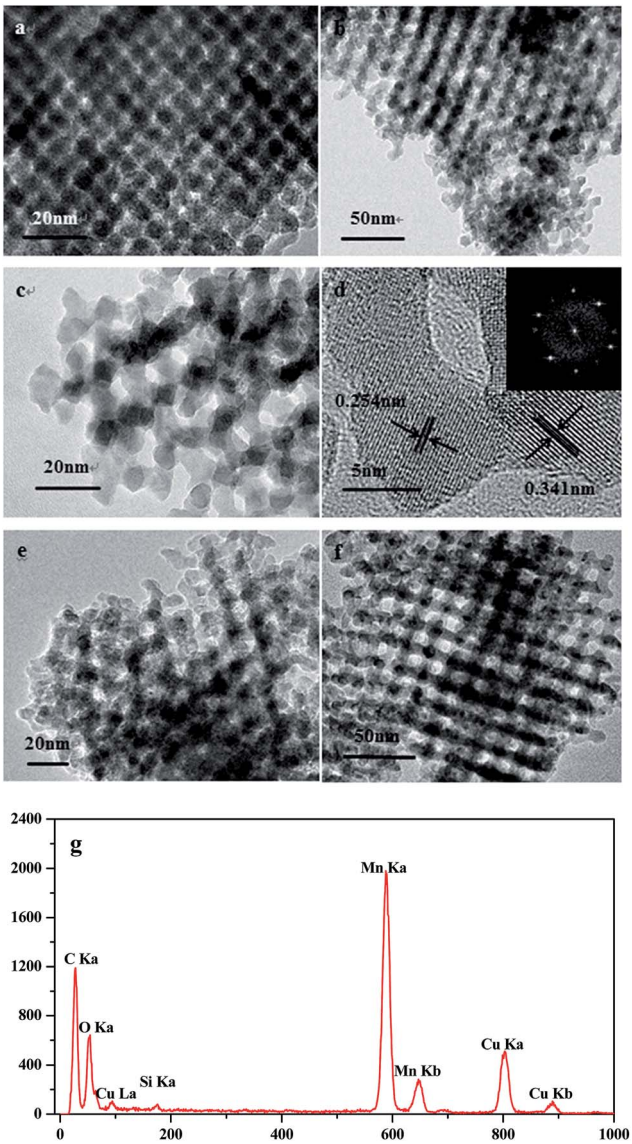

Fig. 1 TEM images of KIT-6 (a), mesoporous MnO_2 (b and c), mesoporous Mn_2O_3 (e) and the used mesoporous MnO_2 (f), HRTEM image (d) of mesoporous MnO_2, and the energy spectrum analysis (EDS) (g) of mesoporous MnO_2.

The broad peak at 1.7–1.8° indexed as (332) plane for mesoporous MnO_2 further demonstrates the relatively ordered mesostructure, which is in good agreement with the TEM results already described. For mesoporous Mn_2O_3, the characteristic reflection of the (211) plane at 2θ value around 1° also can be clearly observed, indicating that mesoporous Mn_2O_3 has been prepared successfully. However, their positions had shifted toward higher angles and there are no other diffraction peaks, suggesting that the mesostructure of Mn_2O_3 is less ordered than mesoporous MnO_2, which may be because of incomplete pore filling of precursor and the relatively high volume shrinkage during the sintering process.[21,22] The *d*-values calculated from the first peak are 92.9 and 84.9 Å, which correspond to the unit cell parameters, a_0, 10.7 and 22.4 nm for mesoporous MnO_2 and Mn_2O_3, respectively. These values are in good agreement with the TEM results.[22,24]

Wide-angle XRD patterns of bulk MnO_2, mesoporous MnO_2 and Mn_2O_3 are shown in Fig. 2b. Peak positions of mesoporous MnO_2 are the same as with bulk MnO_2; however, the diffraction peaks of mesoporous MnO_2 are broader and lower because of the very fine grain size and defect along the channel produced in the decomposition process, suggesting that the obtained mesoporous MnO_2 are nano-size. The diffraction peaks of both bulk MnO_2 and mesoporous MnO_2 can be well indexed to MnO_2 (JCPDS 24-0735).[22] The diffraction peaks of mesoporous Mn_2O_3 can be well indexed to pure Mn_2O_3 (JCPDS 24-0508).[24] For both mesoporous MnO_2 and Mn_2O_3, no peaks were detected from other phases, suggesting that the synthesized mesoporous MnO_2 and Mn_2O_3 are of high purity. The average particle size of bulk MnO_2 is about 36.4 nm based on the Scherrer equation, whereas, here, the average particle sizes of mesoporous MnO_2 and mesoporous Mn_2O_3 were about 7.2 nm and 13 nm, respectively.

The N_2 adsorption–desorption isotherms and the pore diameter distributions of the mesoporous MnO_2, mesoporous Mn_2O_3 and bulk MnO_2 are shown in Fig. 3. Data on the pore size distribution, pore volume and surface area are listed in Table 1. As shown in Fig. 3a, the typical IV type isotherms of mesoporous MnO_2 and mesoporous Mn_2O_3 in the relative pressure range from 0.4 to 0.8 are characteristic of mesostructure with quality of pores inferior to that of the KIT-6 template, which is in good agreement with the results observed from TEM and XRD.[25,26] In addition, a small hysteresis loop in the relative pressure range from 0.8 to 1.0 for mesoporous MnO_2 and mesoporous Mn_2O_3 can be observed, indicating the presence of a small amount of macropores that might originate from the voids between the ordered mesoporous entities.[25] However, the bulk MnO_2 did not exhibit the typical IV type isotherm, indicating that bulk MnO_2 does not have mesoporous channels. Based on the data shown in Fig. 3b, it can be concluded that the pore size distribution of all of the samples is uniform and centered on 3.8 nm.

As shown in Table 1, the mesoporous MnO_2 with a surface area of 129.274 $m^2\ g^{-1}$ and a pore volume of 0.203 $cm^3\ g^{-1}$ are much larger than those of bulk MnO_2 with a surface area of 5.589 $m^2\ g^{-1}$ and a pore volume of 0.006 $cm^3\ g^{-1}$. The mesoporous Mn_2O_3 with a surface area of 78.724 $m^2\ g^{-1}$ and a pore volume of 0.068 $cm^3\ g^{-1}$ are smaller than mesoporous MnO_2,

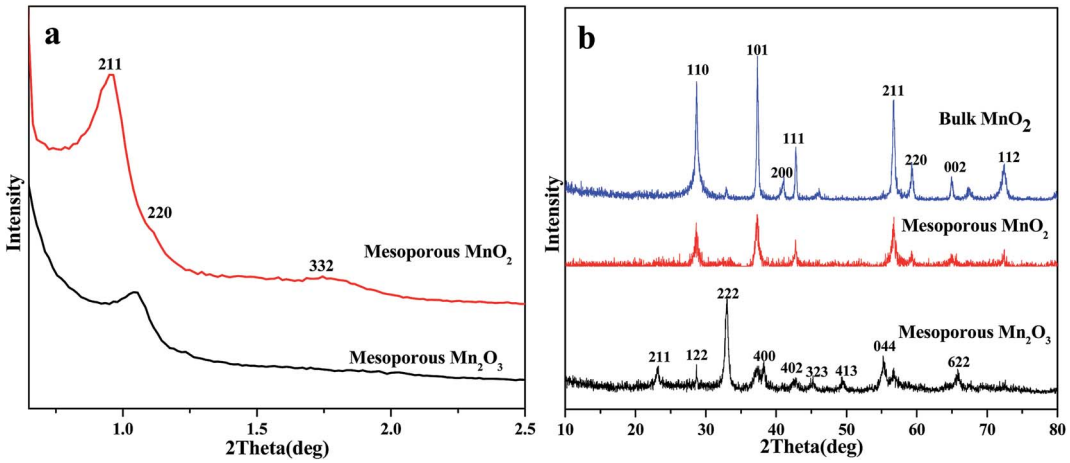

Fig. 2 Low-angle XRD pattern of mesoporous MnO_2 and Mn_2O_3 (a), and wide-angle XRD pattern of mesoporous MnO_2, Mn_2O_3 and bulk MnO_2 (b).

which might be because of collapse of mesostructure caused by incomplete pore filling of precursor and the relatively high volume shrinkage under the higher calcination temperature of Mn_2O_3.[21–23]

As is already known, the surface acidity of the catalyst plays a very important role in low temperature SCR of NO with NH_3.[27] Therefore, to evaluate the acidic site distribution, NH_3-TPD patterns of mesoporous MnO_2, mesoporous Mn_2O_3 and bulk MnO_2 were carried out separately (Fig. 4a). As the thermal stability of the NH_3 molecules coordinated to the Lewis acid sites was higher than that of the NH_4^+ ions bound to the Brønsted acid sites, it can be deduced that the desorption peak at low temperature (below 200 °C) is assigned to NH_4^+ ions bound to Brønsted acid sites and the desorption peaks at high temperature are associated with coordinated NH_3 molecules originating from the Lewis acid sites.[27] Therefore, for bulk MnO_2, the single main peak ranging from 450 to 550 °C indicates a distribution of medium acid sites, which is attributed to the coordinated NH_3 molecules originating from the Lewis acid sites.[28] Three NH_3-TPD peaks of mesoporous MnO_2 can be

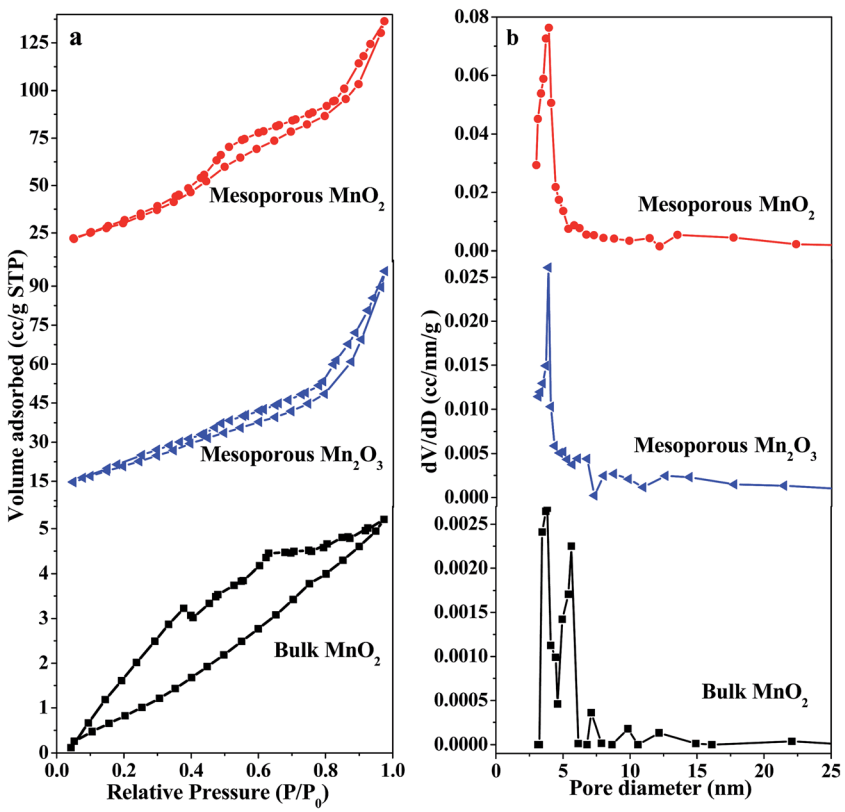

Fig. 3 N_2 adsorption–desorption isotherms (a) and pore diameter distribution (b) of mesoporous MnO_2, mesoporous Mn_2O_3 and bulk MnO_2.

Table 1 Specific area, pore volume and pore diameter distribution of mesoporous MnO_2, mesoporous Mn_2O_3 and bulk MnO_2

Materials	Specific area ($m^2\ g^{-1}$)	Pore volume ($cm^3\ g^{-1}$)	Pore diameter (nm)
Mesoporous MnO_2	116.668	0.203	3.882
Mesoporous Mn_2O_3	78.724	0.068	3.866
Bulk MnO_2	5.589	0.006	3.829

observed obviously. The desorption peak at low temperature ranging from 150 to 200 °C is attributed to the NH_4^+ ions bound to Brønsted acid sites from weak and medium acid sites distributed on the surface of mesoporous MnO_2.[10,27] The two peaks at high temperature ranging from 400 to 550 °C are associated with coordinated NH_3 molecules originating from the Lewis acid sites, which may originate from decomposition of nitrite–nitrate species which are formed from oxidation of ammonia by MnO_2.[27,28] Compared with mesoporous MnO_2 and mesoporous Mn_2O_3, no Brønsted acid sites were obviously observed for bulk MnO_2. The Brønsted acid sites also have an important role in SCR reaction, which may be one of the reasons that the SCR reaction activities of mesoporous MnO_2 and mesoporous Mn_2O_3 are higher than that of bulk MnO_2.[28,29] The NH_3-TPD spectra obtained from mesoporous Mn_2O_3 are similar to that of mesoporous MnO_2, which may be because of similar morphologies. The differences between acid sites on the three catalysts may result from their specific structural features, leading to distinction of the catalytic performance.

To investigate the reducibility of mesoporous MnO_2, mesoporous Mn_2O_3 and bulk MnO_2 catalysts in SCR reaction, the H_2-TPR patterns are shown in Fig. 4b. For bulk MnO_2, three reduction peaks of bulk MnO_2 ranging from 350 to 600 °C can be observed, which are attributed to the reduction of MnO_2 to Mn_2O_3, Mn_2O_3 to Mn_3O_4, and Mn_3O_4 to MnO, respectively.[25,29] For mesoporous MnO_2, the reduction peak ranging from 200 to 600 °C is attributed to the reduction of MnO_2 to Mn_3O_4 and further reduction of Mn_3O_4 to MnO, which is in accordance with a previous study.[25,30] As a comparison, the H_2-TPR peaks of mesoporous Mn_2O_3 show two reduction peaks ranging from 200 to 600 °C: the low temperature reduction peak centered at 360 °C is attributed to reduction from Mn_2O_3 to Mn_3O_4, and the high temperature reduction peak centered at 540 °C is assigned to the further reduction of Mn_3O_4 to MnO, which is in good agreement with a previous report, which indicated that the Mn_2O_3 sample undergoes stepwise reduction of Mn_2O_3 to Mn_3O_4, and Mn_3O_4 to MnO.[10,28] Compared with bulk MnO_2, the first reduction peaks of mesoporous MnO_2 and mesoporous Mn_2O_3 shifted at low temperature, implying that their reduction potentials at low temperatures should be much higher than that of bulk MnO_2.[27,29] The difference between bulk MnO_2 and mesoporous manganese oxide can be explained by considering the effect of small size: the smaller particle size will result in lower reduction temperature, thus, the reduction potentials at low temperatures will be stronger.[29–31] Based on the average particle sizes calculated by XRD patterns, the average sizes of mesoporous MnO_2, mesoporous Mn_2O_3 and bulk MnO_2 are 7.2 nm, 13 nm and 36.4 nm, respectively. Thus, the reduction potential of mesoporous MnO_2 at low temperature is strongest, and the reduction potential of bulk MnO_2 at low temperature is weakest. For mesoporous MnO_2, the small size particles may occur because growth of MnO_2 particles occurred in the pores of the KIT-6 template, thus, the mesoporous MnO_2 particle size will be strictly limited by the mesoporous channels of KIT-6.[12–16] Moreover, the particle size of the bulk MnO_2 is much bigger than that of mesoporous MnO_2 because of the calcination growth. These results indicate that the ordered mesoporous channels changed the particle size and further improved the reduction potentials of samples in SCR removal of NO.

To obtain information about the oxidation states and atomic compositions of manganese and about oxygen species on the catalyst surface, the XPS spectra of Mn 2p, O 1s of mesoporous MnO_2, mesoporous Mn_2O_3 and bulk MnO_2 are shown in Fig. 5, which had been calibrated against the C ls peak standardized at 284.6 eV.[31] From Fig. 5a, two main peaks attributed to Mn $2p_{3/2}$ and Mn $2p_{1/2}$ can be observed in mesoporous MnO_2, mesoporous Mn_2O_3 and bulk MnO_2. After a peak-fitting deconvolution, the Mn $2p_{3/2}$ of mesoporous MnO_2 and bulk MnO_2 can be combined

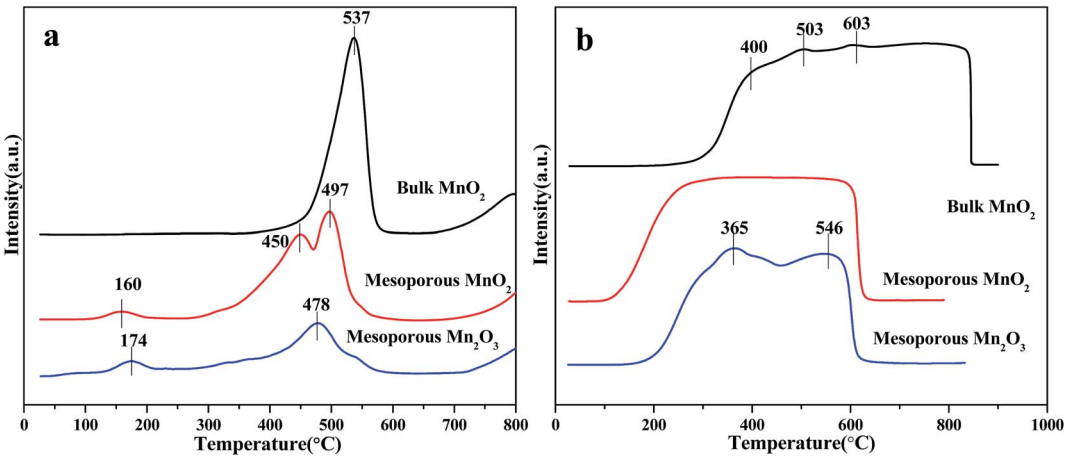

Fig. 4 NH_3-TPD patterns (a) and H_2-TPR patterns (b) of mesoporous MnO_2, mesoporous Mn_2O_3 and bulk MnO_2.

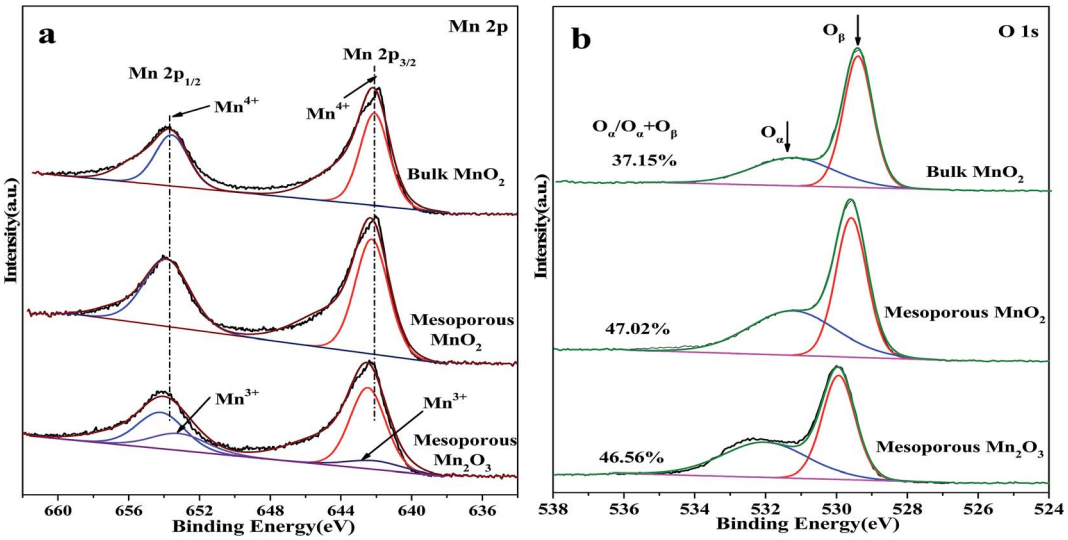

Fig. 5 XPS spectrum of mesoporous MnO_2, mesoporous Mn_2O_3 and bulk MnO_2: (a) Mn 2p, (b) O 1s.

into one peak with Mn^{4+} (642.1–642.2 eV), and the corresponding peaks of mesoporous MnO_2 and bulk MnO_2 in Mn $2p_{1/2}$ also can be combined into one peak with Mn^{4+} (653.5–653.8 eV), indicating that Mn^{4+} is the main valence state of Mn in MnO_2.[32] However, the Mn $2p_{3/2}$ of mesoporous Mn_2O_3 can be separated into two peaks with Mn^{3+} (642.1 eV) and Mn^{4+} (642.4 eV), and the corresponding peaks of Mn $2p^{1/2}$ are located in 653.2 eV (Mn^{3+}) and 654.2 eV (Mn^{4+}).[33]

From Fig. 5b, two kinds of surface oxygen species can be distinguished by performing a peak-fitting deconvolution. The peak at lower B.E. of 528.0–530.0 eV belongs to the surface lattice oxygen (O_β), and the peaks at higher B.E. of 531.0–532.0 eV can be attributed to surface chemisorbed oxygen (O_α), such as the defect oxides or surface oxygen ions bonded to manganese in a low coordinated environment.[33,34] The ratio of $O_\alpha/(O_\alpha + O_\beta)$ in mesoporous MnO_2 (47.02%) was much higher than that in bulk MnO_2. Because the surface chemisorbed oxygen is active in an oxidation reaction, the higher O_α rate will be conducive to reaction of SCR, which can be confirmed by following the results of SCR activity.[34,35] There is no significant difference in the O_α rate between mesoporous MnO_2 and Mn_2O_3, suggesting that the O_α rate has little effect on the difference in SCR activity between mesoporous MnO_2 and Mn_2O_3.

Binding energies and the percent of different valence states for manganese and oxygen determined from deconvoluted XPS spectra are shown in Table 2. It was found that Mn^{4+} is the predominant valence state of Mn; this can be verified from the SCR activity. From Table 2, the Mn^{4+} concentration of mesoporous MnO_2 is higher than that of mesoporous Mn_2O_3, hence Mn^{4+} plays a key role in SCR activity, in good agreement with a previous report.[28,32] This may be one of the reasons that the NO removal efficiency of mesoporous Mn_2O_3 is lower than that of mesoporous MnO_2.

3.2 SCR activity

SCR removal of NO was done with different catalysts: mesoporous MnO_2, mesoporous Mn_2O_3, bulk MnO_2 and commercial VWTi catalyst. As illustrated in Fig. 6, less than 20% NO conversion is obtained below 150 °C using VWTi. However, the NO conversion for VWTi increases quickly to 98% at 300 °C. The highest NO conversion for bulk MnO_2 is 58.35%, with 50% NO conversion being reached below 200 °C. From Fig. 6, the NO conversion ratio with mesoporous MnO_2 is twice that of bulk MnO_2 in the whole temperature window. For mesoporous MnO_2, the NO conversion reached more than 97% in the temperature window ranging from 150 to 250 °C, and the conversion can be increased by up to 100% at 200 °C. Based on the results of N_2 adsorption–desorption, XPS, TPR and TPD, compared with bulk MnO_2, the much higher NO conversion using mesoporous MnO_2 can be attributed to its huge specific surface area, more surface chemisorbed oxygen, high reducibility and strong acid sites.[10,31] The highest NO conversion of mesoporous Mn_2O_3 is 94.35% and the best active temperature

Table 2 Binding energies and the percent of different valence states for manganese and oxygen determined from deconvoluted XPS spectra

	Percent of valence state, % (binding energy, eV)					
Materials	Mn^{4+} $2p_{3/2}$	Mn^{4+} $2p_{1/2}$	Mn^{3+} $2p_{3/2}$	Mn^{3+} $2p_{1/2}$	O_α	O_β
Mesoporous MnO_2	55.24 (642.2)	44.76 (653.8)	—	—	47.02 (531.2)	52.98 (529.6)
Mesoporous Mn_2O_3	48.17 (642.4)	28.35 (654.2)	5.45 (642.1)	10.67 (653.2)	46.56 (532)	53.44 (529.9)
Bulk MnO_2	61.28 (642.1)	38.72 (653.5)	—	—	37.15 (531.3)	37.85 (529.5)

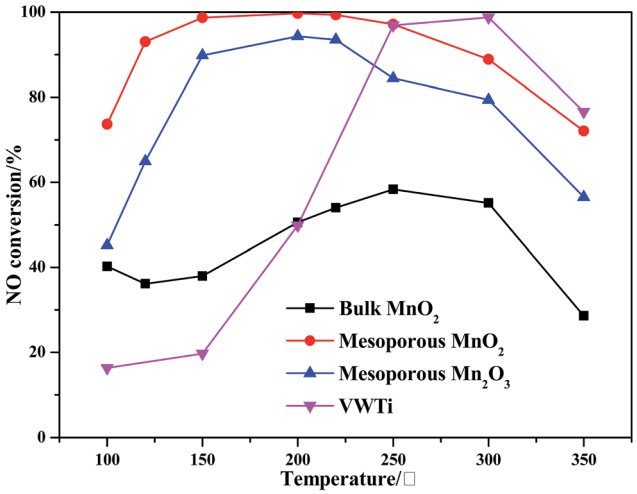

Fig. 6 NO conversion of mesoporous MnO_2, mesoporous Mn_2O_3, bulk MnO_2 and VWTi under the conditions of 500 ppm NO, 500 ppm NH_3, 3% O_2, GHSV of 28 000 h^{-1} and N_2 balance gas.

ranges from 150 to 250 °C, which is a little lower than for mesoporous MnO_2. From the analysis of N_2 adsorption–desorption and XPS, this can be ascribed to the smaller specific surface area and the lower content of Mn^{4+} compared with the mesoporous MnO_2. Therefore, this indicates that specific surface area and oxidation states of manganese can improve the SCR activity of manganese oxide.[9]

3.3 Effect of H_2O and GHSV

Some fraction of water vapor exists in the air, therefore it is important to evaluate the effect of water vapor in the SCR reaction for mesoporous MnO_2. We carried out the SCR reaction with GHSV of 28 000 h^{-1} in the presence of 5% H_2O to test the durability of the catalyst (Fig. 7a). As can be seen, in the absence of 5% H_2O, mesoporous MnO_2 shows high and steady NO conversion of 99% in 200 °C. In the presence of 5% H_2O, the NO conversion decreases to 91% as a result of blocking of some active sites on the catalyst surface.[31,35] After cutting off the H_2O inlet, NO conversion over mesoporous MnO_2 rapidly recovered to 99%, indicating a reversible inhibition effect of H_2O on the SCR activity.

Fig. 7b shows further investigation of the SCR activity with mesoporous MnO_2 as catalyst, with the NO conversion ratio valued in a wider reaction temperature from 100 to 350 °C and GHSV of 28 000–100 000 h^{-1}. The NO conversion decreased with elevated GHSV, because the contact time became shorter and shorter.[27] It was also shown that the GHSV has little influence on SCR activity in the whole temperature window of 100–350 °C. At GHSV of 53 000 h^{-1}, mesoporous MnO_2 still achieves more than 90% conversion at low temperatures ranging from 150 to 250 °C. Even at high GHSV of 100 000 h^{-1}, the NO conversion can reach 90% at 200 °C. Notably, mesoporous MnO_2 still shows more than 95% NO conversion at the wide temperature window of 150–250 °C and higher GHSV of 28 000 h^{-1}.

3.4 *In situ* DRIFT discussion

To further investigate the reaction mechanism, *in situ* DRIFT was conducted (Fig. 8). In this experiment, the mesoporous MnO_2 was first treated with NO + O_2/Ar for 30 min and then purged with Ar for 30 min. NH_3 was introduced at 150 °C, and the DRIFT spectra were recorded as a function of time (Fig. 8a). After NO + O_2 adsorption, three nitrate species were detected, shown by the bands at 1623 cm^{-1} and at 1295 cm^{-1} corresponding to bridging nitrate, the band at 1580 cm^{-1} corresponding to bidentate nitrate, and the band at 1545 cm^{-1} attributed to monodentate nitrate.[35,36] After NH_3 was purged over mesoporous MnO_2, the peak of bidentate nitrate rapidly vanished because of its high reactivity, with the band at 1623 cm^{-1} transforming to a higher band at 1624 cm^{-1} indicating the high stability of bridging nitrate.[36,37] Meanwhile, a great number of NH_3 species were detected, such as hydrogen bonds, coordination to an electron-deficient metal atom (Lewis acid site), dissociation of NH_3 with formation of NH_2 or NH groups, and formation of NH_4^+ at Brønsted acid sites. The

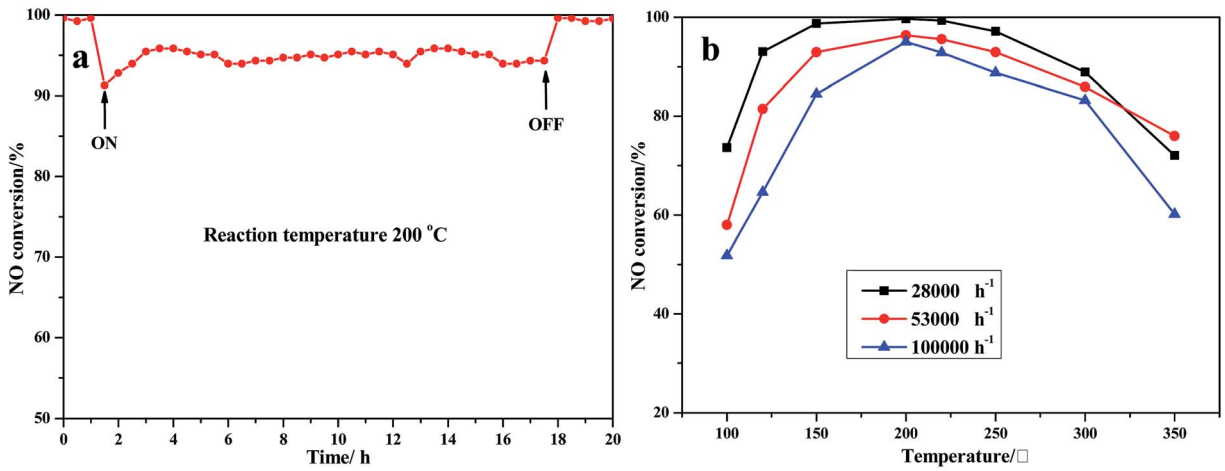

Fig. 7 The effect of H_2O (a) and GHSV (b) on NO conversion for mesoporous MnO_2 at 200 °C. Reaction condition: 500 ppm NO, 500 ppm NH_3, 3% O_2, 5% H_2O (when used), and N_2 balance gas.

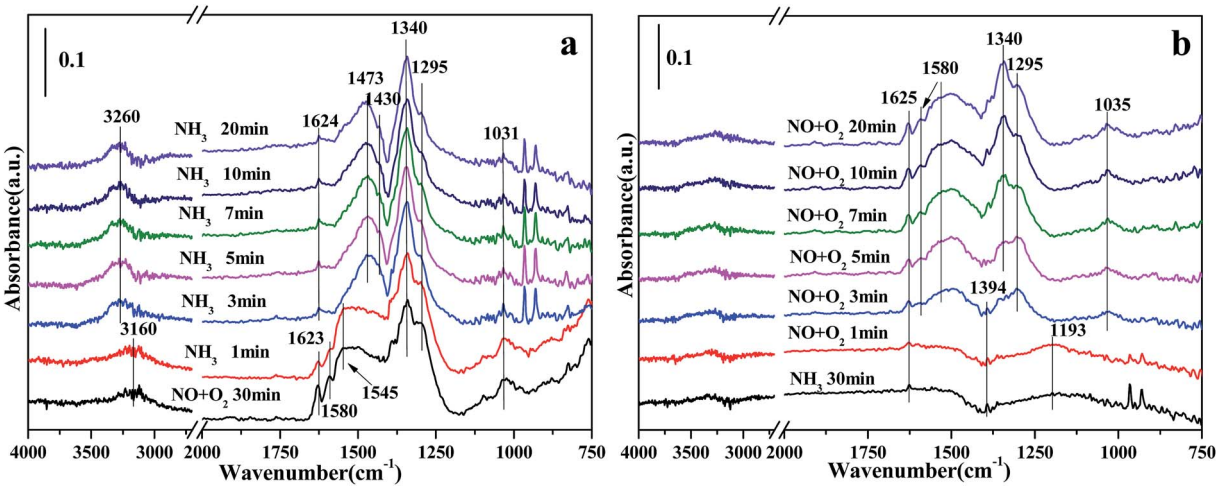

Fig. 8 *In situ* DRIFT spectra of mesoporous MnO_2 between (a) NH_3 and adsorbed NO at 150 °C, (b) NO + O_2 and adsorbed NH_3 species at 150 °C.

features centered at 3160 and 3260 cm^{-1} were attributed to the stretching vibrations of weakly absorbed ammonia species.[35] The band at 1031 cm^{-1} is caused by ammonia hydrogen bonding to the surface oxygen atoms of mesoporous MnO_2, whereas the bands at 1430 and 1473 cm^{-1} are correlated to NH_4^+ ions formed on Brønsted acid sites.[38,39] A new band at 1340 cm^{-1} is quite different from the adsorbed NOx and NH_3 species mentioned previously, assigned to intermediate species from the combination of surface adsorbed NH_3 and NOx species.[40] All the results indicate that reaction between ammonia and nitrate species was unlikely to have occurred, except for reaction between NO_2 and ammonia. The coexistence of ammonia and nitrate species showed that NH_3 and NOx could be adsorbed over different active sites of the catalyst surface.

The *in situ* DRIFT spectra of the reaction between NO + O_2 and pre-adsorbed NH_3 species on the catalyst at 150 °C are displayed in Fig. 8b, conducted in reverse order compared with Fig. 8b. The mesoporous MnO_2 were first treated with NH_3/Ar for 30 min and then purged with Ar for 30 min. When NH_3 was introduced at 150 °C, the spectra were recorded at different times. After NH_3 adsorption, some NH_3 species were observed, including the bands at 1625 cm^{-1} and 1193 cm^{-1} from symmetric and asymmetric deformation vibration of ammonia coordination to Lewis acid sites, and the band at 1394 cm^{-1} correlated to NH_4^+ ions formed on Brønsted acid sites. After NO + O_2 was purged over mesoporous MnO_2, the bands attributed to adsorbed NH_3 species decreased slightly and the main nitrate species began to form on the catalyst surface. The bands centered at 1625 and 1295 cm^{-1} are assigned to bridging nitrate and the band at 1580 cm^{-1} is attributed to bidentate nitrate. A new band at 1340 cm^{-1} can be observed clearly, which was assigned to intermediate species from the combination of surface adsorbed NH_3 and NOx species. All these results indicate that both ionic NH_4^+ and coordinate NH_3 play important roles in reducing NO in SCR reaction.

4 Conclusions

In this study, highly ordered mesoporous MnO_2 and Mn_2O_3 were successfully prepared through nanocasting using KIT-6 as a hard template, and applied in SCR removal of NO with NH_3. The mesoporous MnO_2 could clean approximately 100% NO in a wide temperature window from 150 to 250 °C. Mesoporous Mn_2O_3 and bulk MnO_2 were compared with mesoporous MnO_2 to illustrate the effect of mesostructure and oxidation state of manganese oxide on SCR reaction. From XPS, H_2-TPR, NH_3-TPD and DRIFT, it was found that NO conversion using mesoporous MnO_2 was greater than using bulk MnO_2 because of the huge specific surface area, more surface chemisorbed oxygen, high reducibility and strong acid sites. This indicates that mesostructure has an effect on the specific surface area, surface chemisorbed oxygen, reducibility and acid sites of catalyst, with resulting influence on the SCR reaction. The NO conversion using mesoporous MnO_2 was also higher than using mesoporous Mn_2O_3, attributed to higher Mn^{4+}.

Acknowledgements

The authors gratefully acknowledge the financial support provided by the National Natural Science Foundation of China (21377061), the Asia Research Center in Nankai University (AS1326), the Natural Science Foundation of Tianjin (12JCQNJC05800), and the Key Technologies R&D Program of Tianjin (13ZCZDSF00300) and the assistance provided by Dr Raymond Seekell (University of Notre Dame) in the manuscript preparation and discussion.

Notes and references

1 S. J. Yang, C. X. Liu, H. Z. Chang, L. Ma, Z. Qu, N. Q. Yan, C. Z. Wang and J. H. Li, *Ind. Eng. Chem. Res.*, 2013, **52**, 5601–5610.

2 Y. Peng, J. H. Li, L. Chen, J. H. Chen, J. Han, H. Zhang and W. Han, *Environ. Sci. Technol.*, 2012, **46**, 2864–2869.
3 P. Li, Y. Xin, Q. Li, Z. P. Wang, Z. L. Zhang and L. Zheng, *Environ. Sci. Technol.*, 2012, **46**, 9600–9605.
4 Z. M. Liu, Y. Yi, S. X. Zhang, T. L. Zhu, J. Z. Zhu and J. G. Wang, *Catal. Today*, 2013, **216**, 76–81.
5 K. Zhuang, J. Qiu, F. S. Tang, B. L. Xu and Y. Fan, *Phys. Chem. Chem. Phys.*, 2011, **13**, 4463–4469.
6 D. Fang, J. L. Xie, D. Mei, Y. M. Zhang, F. He, X. Q. Liu and Y. M. Li, *RSC Adv.*, 2014, **4**, 25540–25551.
7 A. Patel, P. Shukla, J. L. Chen, T. E. Rufford, V. Rudolph and Z. H. Zhu, *Catal. Today*, 2013, **212**, 38–44.
8 Z. H. Chen, F. R. Wang, H. Li, Q. Yang, L. F. Wang and X. H. Li, *Ind. Eng. Chem. Res.*, 2012, **51**, 202–212.
9 F. Kapteljn, L. Smgoredjo and A. Andreml, *Appl. Catal., B*, 1994, **3**, 173–189.
10 W. Tian, H. S. Yang, X. Y. Fan and X. B. Zhang, *J. Hazard. Mater.*, 2011, **188**, 105–109.
11 B. Zhi, H. Ding, D. M. Wang, Y. Cao, Y. Zhang, X. Wang, Y. L. Liu and Q. S. Huo, *J. Mater. Chem. A*, 2014, **2**, 2374–2382.
12 Y. J. Sa, K. Kwon, J. Y. Cheon, F. Kleitz and S. H. Joo, *J. Mater. Chem. A*, 2013, **1**, 9992–10001.
13 Q. F. Li, L. X. Zeng, J. C. Wang, D. P. Tang, B. Q. Liu, G. N. Chen and M. D. Wei, *ACS Appl. Mater. Interfaces*, 2011, **3**, 1366–1373.
14 T. Waitz, T. Wagner, T. Sauerwald, C. D. Kohl and M. Tiemann, *Adv. Funct. Mater.*, 2009, **19**, 653–661.
15 J. Rosen, G. S. Hutchings and F. Jiao, *J. Am. Chem. Soc.*, 2013, **135**, 4516–4521.
16 M. Kundu, C. Ng, D. Y. Petrovykh and L. F. Liu, *Chem. Commun.*, 2013, **49**, 8459–8461.
17 J. P. Ma, Q. L. Cheng, V. Pavlinek, P. S. Saha and C. Z. Li, *New J. Chem.*, 2013, **37**, 722–728.
18 R. A. Chandru, S. Patra, C. Oommen, N. Munichandraiah and B. N. Raghunandan, *J. Mater. Chem.*, 2012, **22**, 6536–6538.
19 F. Kleitz, S. H. Choi and R. Ryoo, *Chem. Commun.*, 2003, 2136–2137.
20 J. Y. Luo, J. J. Zhang and Y. Y. Xia, *Chem. Mater.*, 2006, **18**, 5618–5623.
21 X. Z. Cui, J. Zhou, Z. Q. Ye, H. R. Chen, L. Li, M. L. Ruan and J. L. Shi, *J. Catal.*, 2010, **270**, 310–317.
22 Y. Ren, A. R. Armstrong, F. Jiao and P. G. Bruce, *J. Am. Chem. Soc.*, 2010, **132**, 996–1004.
23 Y. X. Liu, H. X. Dai, J. G. Deng, S. H. Xie, H. G. Yang, W. Tan, W. Han, Y. Jiang and G. S. Guo, *J. Catal.*, 2014, **309**, 408–418.
24 F. Jiao, A. Harrison, A. H. Hill and P. G. Bruce, *Adv. Mater.*, 2007, **19**, 4063–4066.
25 J. G. Deng, L. Zhang, H. X. Dai, Y. S. Xia, H. Y. Jiang, H. Zhang and H. He, *J. Phys. Chem. C*, 2010, **114**, 2694–2700.
26 Y. F. Han, F. X. Chen, Z. Y. Zhong, K. Ramesh, L. W. Chen and E. Widjaja, *J. Phys. Chem. B*, 2006, **110**, 24450–24456.
27 C. Wang, L. Sun, Q. Q. Cao, B. Q. Hu, Z. H. Huang and X. F. Tang, *Appl. Catal., B*, 2011, **101**, 598–605.
28 Y. Wan, W. Zhao, Y. Tang, L. Li, H. Wang, Y. Cui, J. Gu, Y. Li and J. Shi, *Appl. Catal., B*, 2014, **148–149**, 114–122.
29 X. Tang, J. Li, L. Sun and J. Hao, *Appl. Catal., B*, 2010, **99**, 156–162.
30 A. Sultana, M. Sasaki and H. Hamada, *Catal. Today*, 2012, **185**, 284–289.
31 B. Thirupathi and P. G. Smirniotis, *J. Catal.*, 2012, **288**, 74–83.
32 C. Yu, G. Li, L. Wei, Q. Fan, Q. Shu and J. C. Yu, *Catal. Today*, 2014, **224**, 154–162.
33 D. Zhang, L. Zhang, C. Fang, R. Gao, Y. Qian, L. Shi and J. Zhang, *RSC Adv.*, 2013, **3**, 8811–8819.
34 H. Chang, X. Chen, J. Li, L. Ma, C. Wang, C. Liu, J. W. Schwank and J. Hao, *Environ. Sci. Technol.*, 2013, **47**, 5294–5301.
35 A. Karami and V. Salehi, *J. Catal.*, 2012, **292**, 32–43.
36 F. Liu and H. He, *J. Phys. Chem. C*, 2010, **114**, 16929–16936.
37 M. Casapu, O. Kröcher, M. Mehring, M. Nachtegaal, C. Borca, M. Harfouche and D. Grolimund, *J. Phys. Chem. C*, 2010, **114**, 9791–9801.
38 W. C. Wang, G. McCool, N. Kapur, G. Yuan, B. Shan, M. Nguyen, U. M. Graham, B. H. Davis, G. Jacobs, K. Cho and X. H. Hao, *Science*, 2012, **337**, 832.
39 D. S. Zhang, L. Zhang, L. Y. Shi, C. Fang, H. R. Li, R. H. Gao, L. Huang and J. P. Zhang, *Nanoscale*, 2013, **5**, 1127–1136.
40 L. Chen, J. Li and M. Ge, *Environ. Sci. Technol.*, 2010, **44**, 9590–9596.